Flow condensation in enhanced tubes: heat transfer and fiction

Shanyue Dai [a], **Wei Li** [a, b, *], **Xiang-Feng Kong** [c,d], **Jiang Jun** [d]
[a] Department of Mechanical and Electrical Engineering, Qingdao University of Science and Technology, Qingdao 266061, China
[b] Department of Energy Engineering, Zhejiang University, Hangzhou 310027, China
[c] Hefei Haier Air Conditioner Co., Ltd., No. 200, Fanhua Avenue, Economic Development Zone, Hefei 230601, Anhui, China
[d] Qingdao Haier Air Conditioner Co., Ltd., Qingdao 266000, China
*Address correspondence to Wei Li, Professor and ASME Fellow in Department of Energy Engineering, Zhejiang University, Hangzhou 310027, China.
E-mail address: weili96@zju.edu.cn. Phone number: 0571-87952244, Fax number: 0571-87952244

Abstract

To investigate the mechanism of condensation heat transfer enhancement of refrigerant R32 in helix micro-fin (HX) tubes, experimental studies were conducted on the heat transfer coefficient (HTC) and frictional pressure drop (FPD) of two HX tubes with different outer diameters (5 mm-HX#1 and 9.52 mm-HX#2) and their corresponding smooth (ST) tubes. The experimental conditions covered saturation temperatures from 36 °C to 48 °C, mass fluxes from 70 to 450 kg m^{-2} s^{-1}, and vapor qualities from 0.1 to 0.9. The results indicate that the heat transfer enhancement factor (EF) of HX#1 and HX#2 reached its maximum at low mass flux (up to 2.93), with the enhancement primarily attributed to increased fluid turbulence and improved condensate drainage. The performance evaluation factor (PEF) also peaked at low mass flux (up to 2.7) and decreased with increasing mass flux. Moreover, the HTC of the HX tubes exhibited weak dependence on mass flux, and for HX#2, the HTC showed an overall decreasing trend as mass flux increased. Based on the experimental data, a new HTC correlation was developed by introducing dimensionless parameters that characterize both flow pattern transitions and geometric structure. The proposed correlation predicted the HTC for HX#1 and HX#2 with mean relative errors (MRE) of +0.7% and −3.2%, respectively, providing a theoretical foundation for the design of enhanced tubes.

Keywords: flow condensation; enhanced heat transfer; pressure drop; prediction correlation.

1. Introduction

Along with the ongoing escalation of global energy requirements and the heightened emphasis on environmental protection, achieving a net-zero energy transition to meet carbon neutrality targets is a key pathway for China to address climate change [1]. In this context, improving the efficiency of refrigeration and heat exchange systems becomes particularly important. Among various strategies, passive surface enhancement has proven effective in optimizing condensation heat transfer inside tubes. Micro-fin structures enlarge the heat transfer area, strengthen turbulence, and induce secondary flows, improving performance significantly. Moreover, micro-fin tubes can withstand the high pressures of environmentally friendly refrigerants, enabling broad applications in air-conditioning, refrigeration, and condensers. In recent years, extensive comparative studies have been conducted between micro-fin tubes and other enhanced tube structures.

Kumar et al. [2] evaluated the condensation characteristics of R-134a in smooth tubes, two types of helix micro-fin tubes, and a novel micro-column tube. Their experimental results showed that the micro-column tube achieved the best condensation heat transfer performance, with heat transfer coefficients 142%–228%, 29%–113%, and 13%–45% higher than those of smooth tubes and the two types of micro-fin tubes, respectively. Li et al. [3][4] systematically assessed hydrophobic, herringbone, dimple, and helix micro-fin tubes. Regarding heat transfer performance, the results revealed that in the low vapor quality region, the herringbone tube exhibited the best performance, while the micro-fin tube performed better compared with its performance in the high vapor quality region, whereas in the high vapor quality region, hydrophobic tubes and dimple tubes (at high mass flux) provided higher heat transfer coefficients. Considering the effect of frictional pressure drop, the performance evaluation factor (PEF) of helix micro-fin tubes gradually surpassed that of dimple tubes as the mass flux increased. Wang et al. [5] further confirmed the excellent heat transfer performance of herringbone tubes, with EF values of 1.76 and 1.38.

In different refrigeration applications, the mass flux of working fluids varies, prompting a series of studies under various operating conditions. In the low-to-medium mass flux range (below 450 kg m^{-2} s^{-1}), Choi et al. [6] evaluated the heat transfer and pressure drop characteristics of R-466A inside helix micro-fin tubes and found that at a mass flux of 300 kg m^{-2} s^{-1}, the EF value reached 1.34 and the PF was 1.37. The EF decreased with increasing mass flux, while the PF showed no significant variation. Lu et al. [7] reported that, compared with smooth tubes, the heat transfer coefficient of R-513A in micro-fin tubes was enhanced by 42% to 74%, with the corresponding pressure drop increasing by 39.11% to 76.63%. They also observed that reducing the tube diameter from 12.70 mm to 9.52 mm significantly increased the heat transfer coefficient by 23.88%–41.62%, accompanied by a rise in pressure drop of 40.79%–71.86%. Kühl et al. [8] highlighted the critical role of fin geometry, showing that finned tubes with 19–48 fins exhibited heat transfer coefficients 9–24 times higher than smooth tubes, and that increasing fin height further enhanced heat transfer. Additionally, Diani et al. [9] and Hirose et al. [10] investigated the heat transfer characteristics of various new refrigerants in small-diameter tubes. Their findings confirmed that micro-fin tubes deliver excellent heat transfer performance for a wide range of working fluids; for instance, for R-32, the heat transfer coefficient can be 2–7 times that of smooth tubes at low mass flux. The two-phase flow data obtained by Hu et al. [11] for internally grooved aluminum tubes with a fin-tip diameter of 5.96 mm provide valuable support for the design of heat exchangers using new refrigerants.

In the medium-to-high mass flux range (above 450 kg m^{-2} s^{-1}), Arkadumnuay et al. [12] reported that micro-fin tubes enhance heat transfer by promoting the formation of annular flow through the disruption of laminar sublayers, with particularly significant effects at low average vapor quality. In these conditions, the heat transfer coefficient increased by 49%–69% compared with smooth tubes, while the frictional pressure drop increased by 87%–120%. Li et al. [13][14] evaluated two helix micro-fin tubes (D_o = 6.35 mm, β = 18°/28°, n_f = 44/54, trapezoidal fins) and found that both EF and PF increased with mass flux and helix angle, and that the comprehensive factor (CHF) was always greater than 1. Based on entropy production analysis, Holagh et al. [15] identified a critical mass flux of 640 kg m^{-2} s^{-1} for 9.52 mm outer diameter tubes under specific conditions, below which micro-fin tubes are more advantageous.

With the growing demand for refrigerant replacement and energy conservation, small-diameter micro-fin tubes have attracted considerable attention in the field of condensation heat transfer due to their high thermal efficiency, compact structure, and reduced refrigerant charge. In recent years, researchers have extensively investigated the condensation performance of such tubes. Diani et al. [17][18] reported that the heat transfer coefficient increases with both mass flux and vapor quality, whereas the frictional pressure drop gradient first increases and then slightly decreases at constant mass flux, and increases with mass flux at constant vapor quality—trends consistent with variations in mass flux and vapor quality. Their measurements showed an EF value of up to 1.45 and a PF of 1.24. Zhang et al. [19] concluded from experiments that the vapor–liquid density difference makes a significant contribution to heat transfer enhancement in small-diameter micro-fin tubes. Khairul Bashar et al. [20] observed that a decrease in tube diameter increases the pressure drop, with PF values ranging from 1.04 to 2.5. Experimental data from Longo et al. [21] indicated that the heat transfer coefficient is highly sensitive to vapor quality and exhibits a non-monotonic variation with operating conditions; EF values reached 3.5–3.6 under certain conditions. Using high-speed visualization, Irannezhad et al. [22] found that annular flow is the most effective regime for heat transfer enhancement and that micro-fin tubes are more prone to flow pattern transitions than smooth tubes. Ubudiyah et al. [23] also confirmed the general trend that the heat transfer performance of small-diameter tubes varies with operating conditions.

Although extensive research has been conducted on the condensation characteristics of small-diameter (≤ 5 mm) micro-fin tubes, the tube geometries reported in the literature differ significantly from those used in the present work, as shown in Table 1. Therefore, it remains of considerable academic value to investigate the heat transfer mechanism for the specific geometry tested in this study. In this study, the condensation of R-32 was examined under operating conditions representative of practical applications: saturation temperatures of 36 °C, 42 °C, and 48 °C; vapor quality from 0.1 to 0.9; and mass flux from 70 to 450 kg m^{-2} s^{-1}. The EF and PEF are introduced to assess the overall performance of the micro-fin tube. Finally, the predictive capability of six classical correlations is evaluated, and based on the most accurate one, a modified correlation is proposed for R-32 condensation in the tested micro-fin tube.

Table 1 Summary of micro-fin tube geometries in recent studies on flow condensation in tubes.

Researcher	Outer diameter D_o (mm)	root diameter D_i (mm)	Helical angle β (°)	Fin height e (mm)	Fin apex angle γ (°)	Number of fin n_f
Diani et al. [17][18]	4	3.4	18	0.12	43	40
Zhang et al. [19]	5	4.6	27	0.12	40	-
Khairul Bashar et al. [20]	2.5	2.18	10	0.1	31	25
Longo et al. [21]	5	4.2	18	0.15	42	40
Irannezhad et al. [22]	5	4.28	30	0.15	-	54
Ubudiyah et al. [23]	3.5	3.2	10	0.1	35	25

2. Experiment details

2.1. Experiment equipment

The system flow diagram of the test platform is presented in Fig. 1. The platform comprises multiple working fluid circulation loops. Based on the type of heat exchange medium, the system can be broadly divided into a primary circulation loop, in which the refrigerant serves as the working medium, and several secondary circulation loops, in which other fluids (water and cooling oil) act as the working media. The experimental apparatus used in this study is described in detail by Li et al. [4].

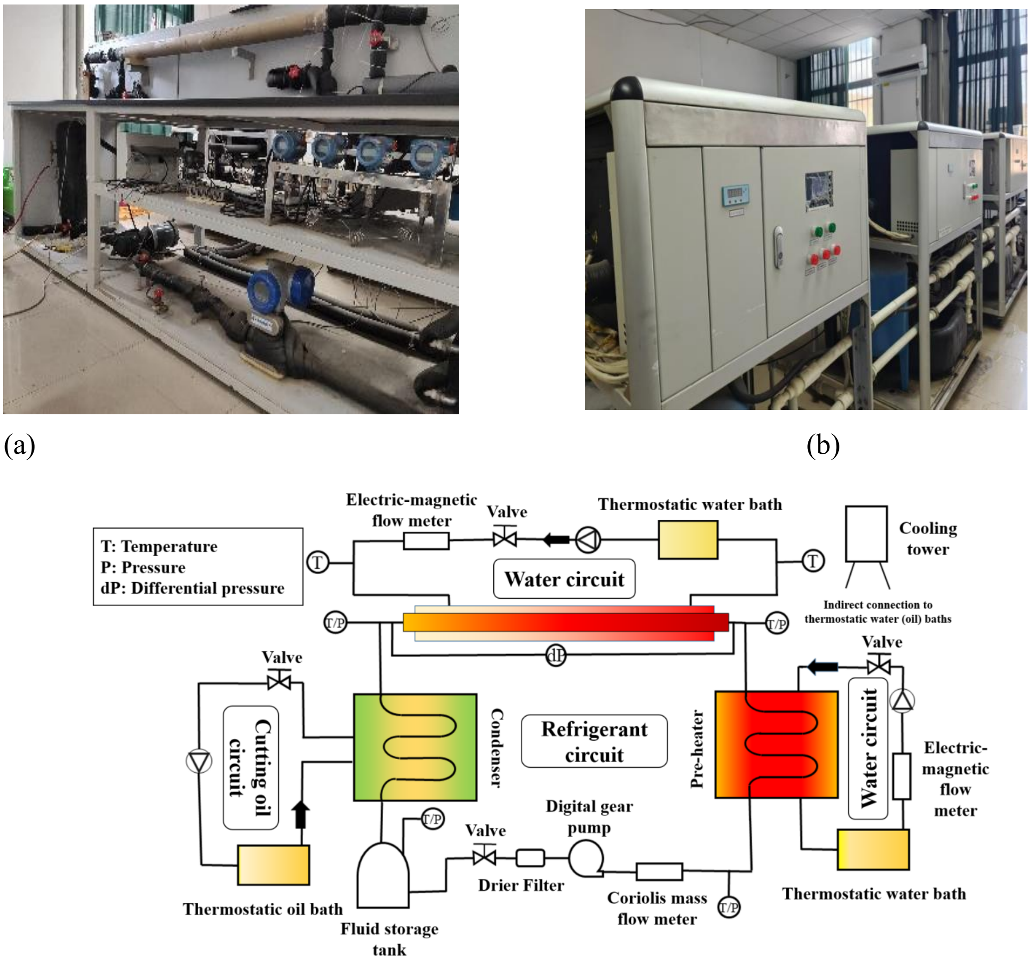

(a) (b)

(c)

Fig.1. Test bench (a) Front view (b) Rear view (c) System flowchart of testing platform.

In this experimental study, four copper heat transfer tubes were tested: a smooth tube (ST#1) and a helix micro-fin tube (HX#1) with an outer diameter of 5.0 mm, as well as a smooth tube (ST#2) and a helix micro-fin tube (HX#2) with an outer diameter of 9.52 mm. The fin cross-section of HX#1 is triangular, whereas that of HX#2 is trapezoidal. Fig. 2 presents both the actual photographs and the three-dimensional microscopic structures of the micro-fin tubes. The detailed geometric parameters of the four tubes are summarized in Table 2.

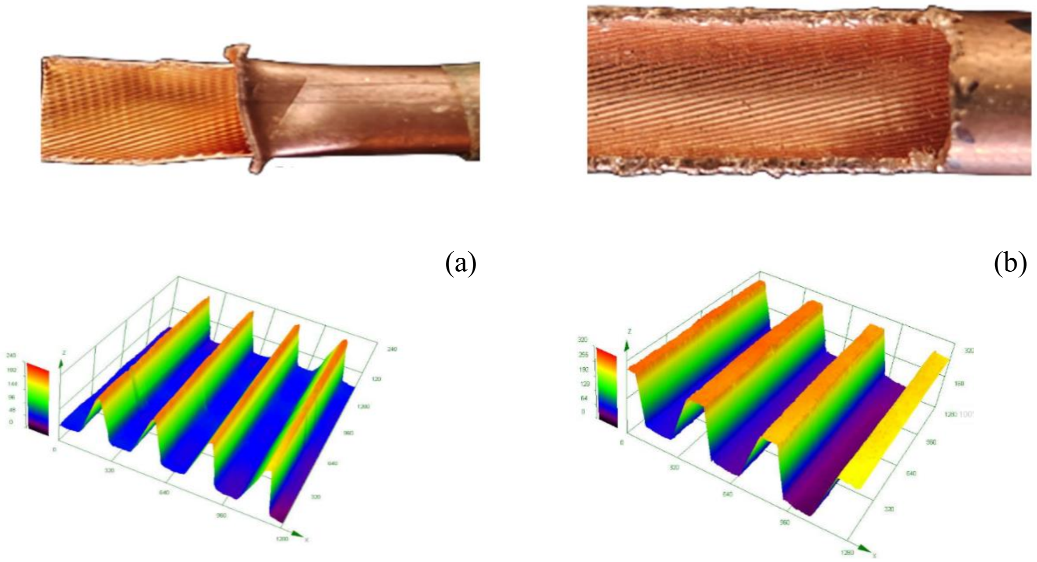
(a) (b)

Fig. 2. Photographs and three-dimensional views of the enhanced tubes: (a) HX#1, (b) HX#2.

Table 2 The geometric parameters of the tubes.

/	D_o (mm)	D_i (mm)	W_t (mm)	e (mm)	p_t (mm)	β (°)	γ (°)	Ar	L (m)
ST#1	5	4.6	0.2	-	-	-	-	1	2
HX#1	5	4.6	0.2	0.15	0.3	35	45	1.66	2
ST#2	9.52	8.3	0.6	-	-	-	-	1	2
HX#2	9.52	8.3	0.6	0.24	0.42	35	45	1.93	2

The structural details of HX#1 are presented in Fig. 2(a). It has a fin height of 0.15 mm, a fin pitch of 0.30 mm, a helix angle of 35°, a fin apex angle of 45°, and the effective heat transfer area was increased by 66% compared with ST#1. The details of HX#2 are shown in Fig. 2(b), featuring a fin height of 0.24 mm, a fin pitch of 0.42 mm, a helix angle of 35°, a fin apex angle of 45°, and an effective heat transfer area increased by 93%. Apart from minor variations introduced by the manufacturing process, all enhanced helix micro-fin tubes share identical surface parameters.

2.2. Experimental conditions

In this experimental study, the effects of mass flux, saturation temperature, and tube diameter (for different internal surface structures) on the HTC and PDF were investigated under conditions of saturation temperatures of 36°C, 42°C, and 48°C, with an inlet vapor quality of 0.8, an outlet vapor quality of 0.2, and a mass flux ranging from 70 to 470 kg m^{-2} s^{-1}. At a constant mass flux of 300 kg m^{-2} s^{-1} and a fixed vapor quality difference of 0.2 between the inlet and outlet, the influence of average vapor quality on HTC and PDF was further examined. Finally, the EF and PEF were introduced to assess the flow condensation heat transfer characteristics in enhanced tubes, with the experimental conditions covering the entire range described above.

3. Data reduction

The inlet vapor quality (x_{in}) and outlet vapor quality (x_{out})of the refrigerant in the test section were determined using Eqs. (1) and (2), respectively.

$$x_{in} = \frac{Q_{w,ph} - c_{p,ref,ph} m_{ref,ph} (T_{sat} - T_{ref,ph,in})}{m_{ref,ph} h_{lv}} \tag{1}$$

$$x_{out} = x_{in} - \frac{Q_{w,exp}}{(m_{ref,exp} \cdot h_{lv})} \tag{2}$$

Where $c_{p,ref,ph}$ is the specific heat capacity of the refrigerant in the preheating section; $T_{ref,ph,in}$ is the inlet temperature of the refrigerant side in the preheating section; $m_{ref,ph}$ is the mass flow rate of the refrigerant in the preheating section; and h_{lv} is the latent heat of the refrigerant in the test section.

In terms of heat transfer performance, the primary focus of this study is the heat transfer coefficient of the refrigerant inside the test section tube (h_i), which is calculated using Eq. (3):

$$h_i = \frac{1}{A_i \left[\frac{LMTD}{Q_{w,exp}} - \frac{1}{h_o A_o} - \frac{D_o \ln{(D_o/D_i)}}{2\lambda A_o} \right]} \tag{3}$$

Where A is the heat transfer area of the test tube; h_o is the water-side heat transfer coefficient; and λ is the thermal conductivity of copper.

In terms of pressure drop, the primary focus of this study is the frictional pressure drop gradient of the refrigerant inside the test section tube (ΔP_f), which is calculated using Eqs. (4) and (5):

$$\Delta P_f = \frac{\Delta P_{to} - \Delta P_a}{L} \tag{4}$$

$$\Delta P_a = {G_{ref}}^2 \left\{ \left[\frac{x^2}{\rho_v \varepsilon_{ra}} + \frac{(1-x)^2}{\rho_l (1-\varepsilon_{ra})} \right]_{out} - \left[\frac{x^2}{\rho_v \varepsilon_{ra}} + \frac{(1-x)^2}{\rho_l (1-\varepsilon_{ra})} \right]_{in} \right\} \tag{5}$$

Where ΔP_{to} is the total pressure drop, directly measured by the pressure transducers; ΔP_a is the acceleration pressure drop caused by density variations of the refrigerant during condensation; and ε_{ra} is the void fraction, determined using the correlation proposed by Rouhani and Axelsson [24], which applies to different flow patterns.

The enhancement factor (EF) and performance evaluation factor (PEF) are determined by Eq. (6):

$$EF = \frac{h_{TT}}{h_{st}} \tag{6a}$$

$$PEF = \frac{h_{TT}/h_{ST}}{\Delta P_{TT}/\Delta P_{ST}} \tag{6b}$$

Where h_{TT} and h_{ST} are the heat transfer coefficients of the test tube (TT) and smooth tube

(ST), respectively.

The experimental results were subjected to an uncertainty analysis using the methodology described by Moffat [25], with the detailed data summarized in Table 3. The HTC's uncertainty was determined to be ±9.21%, indicating a high level of accuracy. The specific procedures for data reduction and uncertainty analysis can be found in the work of Ma et al. [26].

Table 3 Uncertainties of measured and calculated parameters.

Parameters	Uncertainty
L (mm)	$\pm 0.05\%$
D_i (mm)	$\pm 0.23\%$
T (K)	$\pm 1.37\%$
P (bar), range: 40 bar	$\pm 0.031\%$
m_{ref} (kg h^{-1}), range: 0-70 kg/h	$\pm 0.10\%$
m_w (L min^{-1}), range: 0-12 L/min	$\pm 0.17\%$
A (m^2)	$\pm 0.22\%$
G (kg m^{-2} s^{-1})	$\pm 0.53\%$
x	$\pm 2.70\%$
h (W m^{-2} K^{-1})	$\pm 9.21\%$
ΔP_f (kPa m^{-1})	$\pm 3.78\%$

4. Results and discussion

4.1. Feasibility analysis of the experiment

The following tests were conducted to confirm the reliability of the experimental data. Fig. 3(a) shows the single-phase heat balance of the test sections used in this study—including ST#1, ST#2, HX#1, and HX#2—under the specific experimental conditions of this study (T_{sat} = 36°C, x_{in} = 0.8, x_{out} = 0.2, and G_{ref} ranging from 70 to 450 kg m^{-2} s^{-1}). The results indicated that heat loss was less than 6%. Fig. 3(b) presents repeated condensation tests on ST#1 under the same conditions, demonstrating reproducibility within a 3% random error. Both tests confirmed good consistency, validating the experimental data obtained under these conditions.

4.2. Flow patterns analysis

Before presenting the experimental results, it is essential to identify the flow patterns associated with the experimental conditions. The flow pattern map developed by El Hajal et al. [27], which employs the logarithmic mean void fraction (LMe) method, was adopted in this study. According to Liu et al. [28], this method provides the highest prediction accuracy for void fraction behavior under various operating conditions. In the model of El Hajal et al. [27], the flow patterns are classified into fully stratified flow, stratified-wavy flow, intermittent flow, annular flow, mist flow, and bubbly flow. The proposed map was successfully compared with several flow pattern observations and alternative transition methods. The map demonstrated remarkably high accuracy when benchmarked against a database comprising test data from nine independent laboratories. Subsequent visualization studies further confirmed its validity, showing excellent agreement with observed flow patterns [29].

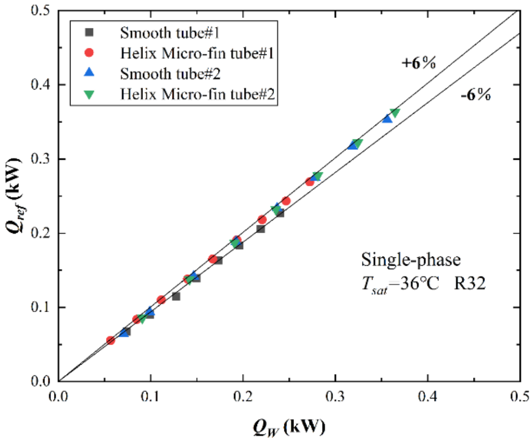

(a)

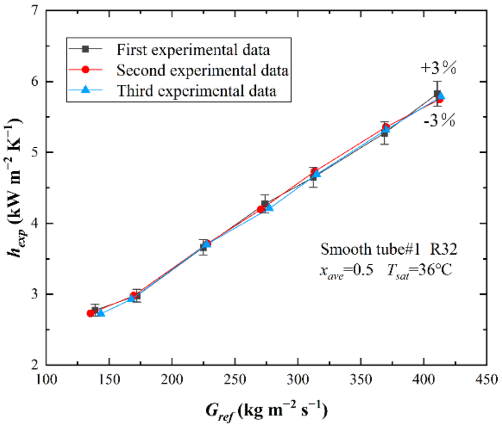

(b)

Fig. 3. Experimental feasibility analysis (a) The verification of heat balance, (b) Repetitive experiment.

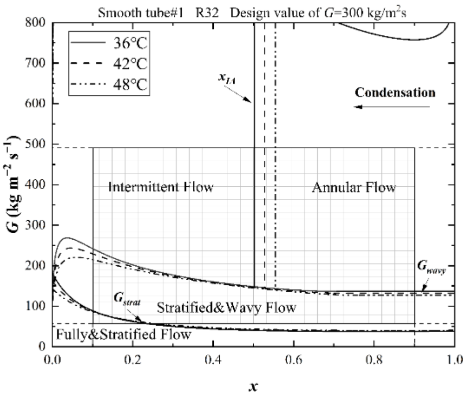

Fig. 4. Prediction of flow patterns of R32 in a smooth tube with an outer diameter of 5 mm.

Fig. 4 presents the flow pattern map calculated under the experimental conditions of this study (refrigerant: R32; mass flux: 300 m^{-2} s^{-1}; tube: ST#1). The rectangular grid region in the figure indicates the range of experimental conditions. During condensation, the incoming saturated vapor develops into two possible flow configurations: (i) annular flow, in which a thin condensate film forms along the tube wall, or (ii) stratified or stratified-wavy flow, where a liquid layer accumulates at the bottom of the tube while a gravity-controlled condensate film forms along the upper wall. Consequently, dryout does not occur during condensation. Therefore, mist and bubbly flow are not further discussed in this study. As shown in Fig. 4, the transition curve labeled G_{wavy} extends horizontally to a vapor quality of 1.0 once its minimum value is reached, indicating that under high vapor quality conditions, the refrigerant flow at the tube inlet directly develops into either stratified-wavy flow or annular flow, depending on whether the mass flux is lower or higher than G_{wavy}. Moreover, it was observed that as the tube diameter decreases, the G_{wavy} boundary shifts to lower values. In summary, the present analysis of flow regime transitions focuses on annular flow, stratified-wavy flow, and intermittent flow.

Hurlburt and Newell [30] were the first to propose that the transition between stratified-wavy flow and annular flow can be characterized by a Froude rate (Ft). Liebenberg et al. [31] combined experimental data and performed a logarithmic regression to derive an equation describing the variation of the Lockhart-Martinelli parameter (X_{tt}) with Ft. Based on this equation, they corrected x_{IA} (the vapor quality at the transition from annular flow to intermittent flow) to account for differences in condensation flow transition criteria between smooth tubes and micro-fin tubes. Following the approach of Liebenberg et al. [31], the current authors applied the same correction—setting X_{tt} to 0.602—which is expressed by Eq. (7):

$$x_{IA} = \left\{\left[0.566\left(\frac{\rho_V}{\rho_L}\right)^{-\frac{5}{9}}\left(\frac{\mu_L}{\mu_V}\right)^{-\frac{1}{9}}\right] + 1\right\}^{-1} \tag{7}$$

The vapor quality determined by Eq. (15) defines the transition between intermittent flow and annular flow in micro-fin tubes. Using Eq. (15), the transition vapor quality for helix micro-fin tubes with R32 is found to be 36.04%. Consequently, the transition vapor quality shifts from approximately 52.79% in smooth tubes (see Fig. 5) to 36.04% in micro-fin tubes, accurately indicating that the transition from annular flow to intermittent flow during condensation in micro-fin tubes is delayed by 16.75%. The influence of the micro-fin structure on altering the flow field, enhancing heat transfer relative to smooth tubes, and increasing pressure drop will be discussed in detail in the following subsections, based on the experimental data.

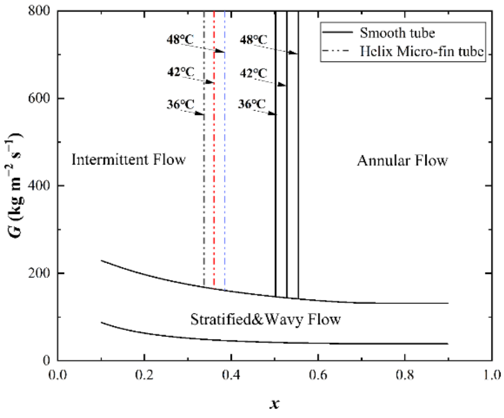

Fig.5. The annular-to-intermittent transition line inside the ST and HX tubes.

4.3. Effects of mass flux, saturation temperature, and average vapor quality

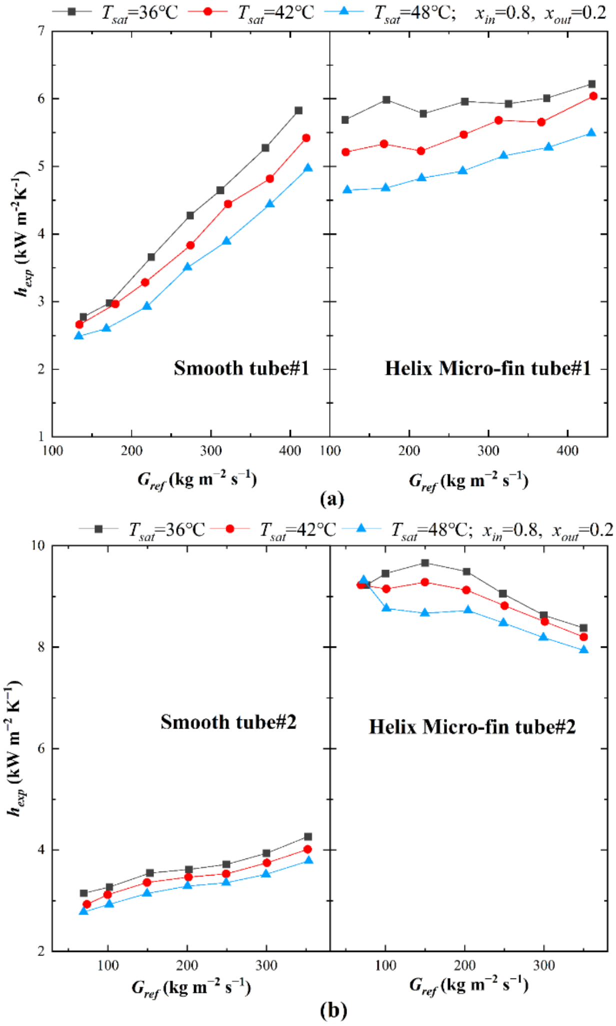

Fig. 6. Variation of condensation heat transfer coefficients with mass flux at different saturation temperatures in tubes (a) ST/HX#1, (b) ST/HX#2.

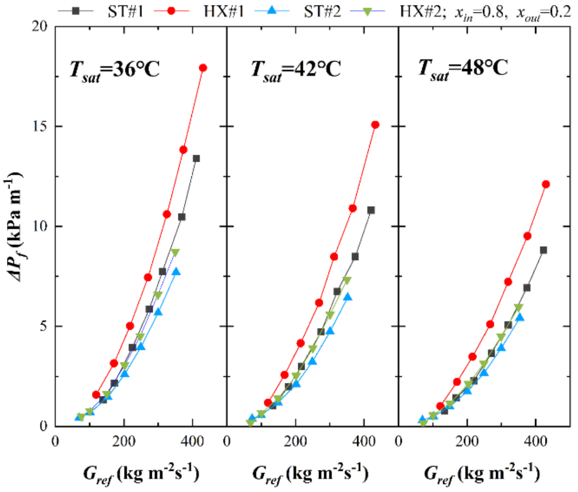

Fig. 7. Comparison of friction pressure drop in tubes at saturation temperatures of 36℃, 42℃, and 48℃ for different tube types under different mass fluxes.

4.3.1. Effects of mass flux

Fig. 6 illustrates the variation of the condensation heat transfer coefficient with mass flux for the four test tubes under specified conditions (T_{sat}: 36°C, 42°C, 48°C; $x_{in} = 0.8$, $x_{out} = 0.2$). It is evident that for both smooth tubes (ST#1, ST#2) and helix micro-fin tubes (HX#1), the heat transfer coefficient increases monotonically as mass flux rises. This trend results from the higher refrigerant mass flux providing greater heat transfer capacity and inducing shifts in flow patterns. At moderate to high mass fluxes, annular and intermittent flow regimes progressively dominate, with the shear force exerted by the vapor phase refrigerant on the liquid film becoming the controlling factor. This causes the liquid film to thin, reduces thermal resistance, and consequently enhances convective heat transfer.

It is worth noting that HX#2 (Fig. 6(b)) exhibits a distinct trend: in the low mass flux region ($G_{ref} < 150$ kg m^{-2} s^{-1}), its heat transfer coefficient shows little sensitivity to changes in mass flux, whereas at higher mass fluxes, a slight decline is observed. This behavior was confirmed through repeated experiments, thereby ruling out the possibility of random errors. The underlying reason could be that for HX#2, which has a larger tube diameter, at low mass fluxes, the relatively low (p_t/e) ratio leads to a stable liquid drainage effect primarily governed by gravity, with the fins causing moderate disturbance to the liquid film and weak surface tension effects. As the mass flux increases further, the liquid phase refrigerant experiences stronger surface tension forces, causing the fins to become progressively submerged by the liquid film. This submersion diminishes the fins' disturbance effect and increases the thermal resistance, ultimately resulting in a slight degradation of the heat transfer coefficient.

Fig. 7 illustrates the variation of the frictional pressure drop gradient with mass flux for the heat exchangers with different tube types. As illustrated, the frictional pressure drop for all test tubes increases significantly with rising mass flux, with HX#1 exhibiting the most pronounced increase, reaching up to 16.35 kPa m^{-1}. The reason is that an increase in mass flux directly enhances the overall flow velocity. and Reynolds number of the two-phase refrigerant inside the tube, thereby intensifying both the shear interaction between the vapor and liquid layers and the friction between the fluid and the tube wall. Furthermore, an increased flow velocity enhances the velocity differential between the two phases, which aggravates interfacial wave fluctuations and consequently results in greater energy dissipation and pressure drop. Additionally, it was observed that as mass flux increases, the frictional pressure drop of ST#1 becomes significantly higher than that of HX#2, indicating that the effect of tube diameter variation on pressure drop should not be overlooked.

4.3.2. Effect of saturation temperature

Fig. 6 illustrates the condensation heat transfer coefficients of refrigerant R32 in all tested tubes at different saturation temperatures, under conditions of an average vapor quality of 0.5 and a mass flux ranging from 70 to 450 kg m^{-2} s^{-1}. When the saturation temperature dropped from 48°C to 36°C, the heat transfer coefficients of ST#1, HX#1, ST#2, and HX#2 increased on average by 17.54%, 19%, 13.2%, and 6.4%, respectively. This phenomenon is primarily attributed to the saturation temperature-dependent variation of the physical properties of R32, as detailed in Table 4.

Table 4 Thermophysical properties of refrigerant R32 at different saturation temperatures (36 °C, 42 °C, and 48 °C).

T_{sat} (°C)	P_{sat} (kPa)	ρ (kg m^{-3})		h (kJ kg^{-1})		μ (10^{-5} Pa s)		λ (W m^{-1} K^{-1})		σ (10^{-3} N m^{-1})	h_{lat} (kJ kg^{-1})
		l	v	l	v	l	v	l	v		
36	2245.4	912.37	65.211	267.34	514.17	9.98	1.35	0.117	0.175	5.08	246.83
42	2601.4	882.96	77.684	279.84	511.82	9.26	1.4	0.113	0.193	4.2	232
48	2998.9	850.77	92.786	292.95	508.48	8.55	1.45	0.109	0.218	3.34	215.54

This trend can be attributed to several factors. First, a decrease in saturation temperature increases the latent heat by 31.29 kJ kg^{-1}, allowing a unit mass of refrigerant to release more heat during phase change. Second, the density difference between the vapor and liquid phases increases by 89.175 kg m^{-3}, which intensifies shear and interfacial disturbance, thereby enhancing overall heat transfer. Furthermore, although the thermal conductivity of the vapor phase decreases slightly, the liquid-phase thermal conductivity—an order of magnitude higher—further increases, improving the overall thermal conductivity of the two-phase refrigerant. In addition, the increase in surface tension promotes the formation of a thinner liquid film, thereby reducing conductive thermal resistance. From the perspective of flow pattern transition (Fig. 5), a lower saturation temperature delays the shift from annular flow to intermittent flow (x_{IA} decreases), altering the flow regime that dominates heat transfer in the medium- and high-mass flux regions. The combined influence of these factors results in an overall enhancement of the condensation heat transfer coefficient.

As shown in Fig. 7, the frictional pressure drop decreases with increasing saturation temperature in the high- and medium-mass-flux regions, whereas this effect is negligible in the low-mass-flux region. This behavior can be explained as follows: at higher mass fluxes, when the saturation temperature increases from 36 °C to 48 °C, the liquid-phase viscosity decreases significantly (from 9.98×10^{-5} Pa s to 8.55×10^{-5} Pa s). In intermittent or annular flows dominated by shear forces, this reduction in viscosity weakens the frictional dissipation between the two-phase refrigerant and both the tube wall and the vapor–liquid interface, thereby reducing the pressure drop. In contrast, at low mass fluxes, where the flow is gravity-dominated (stratified-wavy flow) and shear forces are relatively weak, variations in thermophysical properties exert a much smaller influence on the pressure drop.

4.3.3. Effect of average vapor quality

As shown in Fig. 8(a), the variation of the HTC with average vapor quality at a constant mass flux of 300 kg m^{-2} s^{-1} is presented for the four tested tubes. The results indicate that the sensitivity to average vapor quality differs among tubes with different internal surface structures, while the overall trend exhibits a proportional relationship with the variation of vapor quality. The increase was most pronounced in tube HX#1, with the heat transfer coefficient rising by an average of 487.4 W m^{-2} K^{-1} for every 0.1 increment in average vapor quality, whereas tube ST#2 exhibited a more moderate increase of approximately 201.3 W m^{-2} K^{-1}. The underlying physical mechanism can be explained as follows: at a relatively high mass flux of 300 kg·m^{-2}·s^{-1}, with the increase in average vapor quality, the flow pattern of the two-phase refrigerant gradually shifts from intermittent flow (characterized by a thick liquid film where thermal resistance is dominated by conduction) to annular flow (characterized by a thinner liquid film where convective heat transfer is enhanced). At the same time, the significantly increased vapor velocity intensifies the shear and disturbance at the vapor–liquid interface, which not only further thins the liquid film but also enhances mixing and convection within the two-phase refrigerant, thereby synergistically improving the overall heat transfer performance. Experimental data further indicate that this mechanism is amplified in small-diameter tubes and spiral micro-fin structures, rendering them more sensitive to changes in vapor quality. Collectively, these findings suggest that in engineering practice, optimizing the operating vapor quality can maximize heat transfer performance.

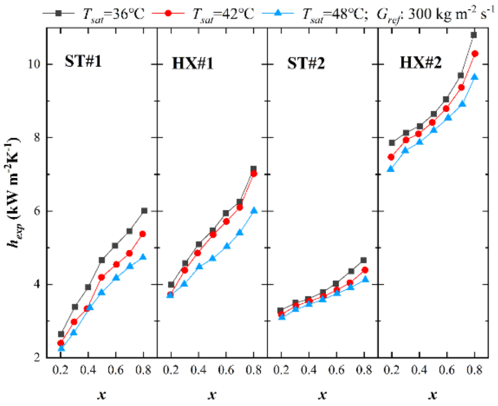

(a)

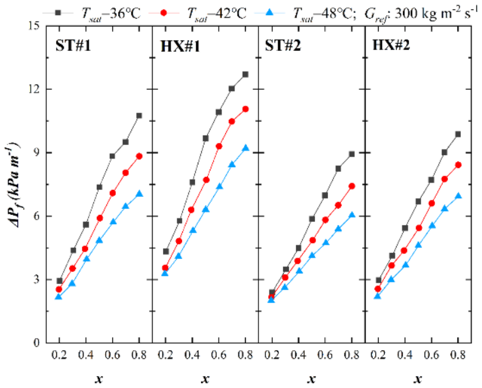

(b)

Fig. 8. Condensation performance of 5 mm and 9.52 mm tubes at various average vapor qualities and saturation temperatures: (a) HTC, (b) FPD.

As shown in Fig. 8(b), the frictional pressure drops of all tube types exhibit similar values at low average vapor quality, while the differences among them gradually enlarge as the average vapor quality increases. Overall, the frictional pressure drop shows an increasing trend. The fundamental cause of the pressure drop increase is that, as the average vapor quality rises, both the vapor-phase volume fraction and the slip velocity between the vapor and liquid phases increase, making shear stress at the vapor–liquid interface the dominant factor and causing it to rise sharply. Notably, at high vapor qualities ($x > 0.7$), the rate of increase in frictional pressure drop slightly diminishes. This behavior can be attributed to the stabilization of the flow structure at high vapor qualities, where condensation occurs without dryout, and the vapor phase forms the core while the liquid phase exists as a thin film or entrained droplets. Consequently, the sensitivity of interfacial shear–dominated friction to changes in vapor quality decreases, and its growth approaches saturation. This characteristic also highlights the key differences in the pressure drop mechanisms between condensation and evaporation in the high vapor quality regime.

4.4. Effect of tube diameter

As shown in Fig. 9, the effect of tube diameter on the condensation heat transfer coefficient of smooth and helix micro-fin tubes reveals the fundamental differences in their dominant mechanisms. For smooth tubes, the impact of tube diameter is closely related to mass flux, with a clear performance reversal point. In the low-to-medium mass flux region, where gravity predominates, the larger tube diameter (9.52 mm) exhibits superior performance due to the more effective drainage of the upper liquid film under gravitational forces. However, in the medium-to-high mass flux region, the governing mechanism gradually shifts to shear force dominance, and the performance of small tube diameters (5 mm) rapidly improves, surpassing that of larger diameters. This is because, in smaller diameters, the reduced flow space shortens the distance between the rapidly moving vapor core and the circumferential liquid film, enhancing both the efficiency and uniformity of interfacial shear forces. Additionally, the thinner liquid film facilitates enhanced momentum and heat transfer toward the boundary layer near the wall. In contrast, the heat transfer performance of large-diameter (9.52 mm) helix micro-fin tubes is significantly superior to that of small-diameter tubes under all test conditions, with heat transfer coefficients 1.51 to 1.97 times higher than those of small-diameter tubes (5 mm). This phenomenon indicates that the heat transfer performance is synergistically dominated by multiple enhancement mechanisms induced by the geometric structure. The core advantage lies in the strong secondary swirl induced by the spiral fins, which efficiently drives the condensate from the top of the fins to the grooves at the base, ensuring that the main heat transfer surface remains covered by a thin liquid film. Furthermore, the spiral structure favors flow pattern distribution, delaying the transition from annular flow to intermittent or stratified-wavy flow, thereby maintaining a higher heat transfer coefficient across a wider range of vapor qualities. Therefore, the comprehensive performance advantages of large-diameter tubes result from the synergistic effects of multiple mechanisms, including increased surface area, swirl-enhanced liquid discharge, surface tension synergy, and flow pattern redistribution. These geometrically induced enhancements far outweigh the negative effects of increased tube diameter, such as reduced shear force. Based on the above analysis, the heat transfer performance of smooth tubes with different diameters depends on the dynamic transition of the dominant mechanisms. The performance of micro-fin tubes, on the other hand, is determined by multiple enhancement mechanisms, such as surface area, swirling, and surface tension, induced by the geometric structure. In this case, a design that fully exploits the advantages of the geometric structure is the key to maximizing performance.

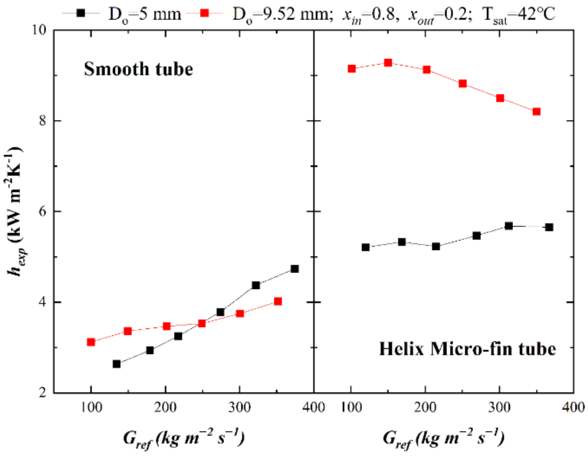

Fig. 9. Heat transfer coefficients of tubes with different diameters but identical surface structures under the same operating conditions.

As shown in Fig. 7, small diameters exhibit significantly higher frictional pressure drops compared to larger diameters. According to the Reynolds number definition, smaller diameters exhibit higher Reynolds numbers at the same mass flux, leading to a higher likelihood of the flow entering the turbulent zone. This increase in wall shear stress leads to higher friction losses. In small diameters, the flow cross-sectional area of the entire tube is smaller, and the boundary layer occupies a relatively larger proportion, meaning that the interaction area between the boundary layer and the main flow area is larger. As a result, the shear stress between fluid layers increases, further contributing to the pressure drop.

4.5. Effect of tube type

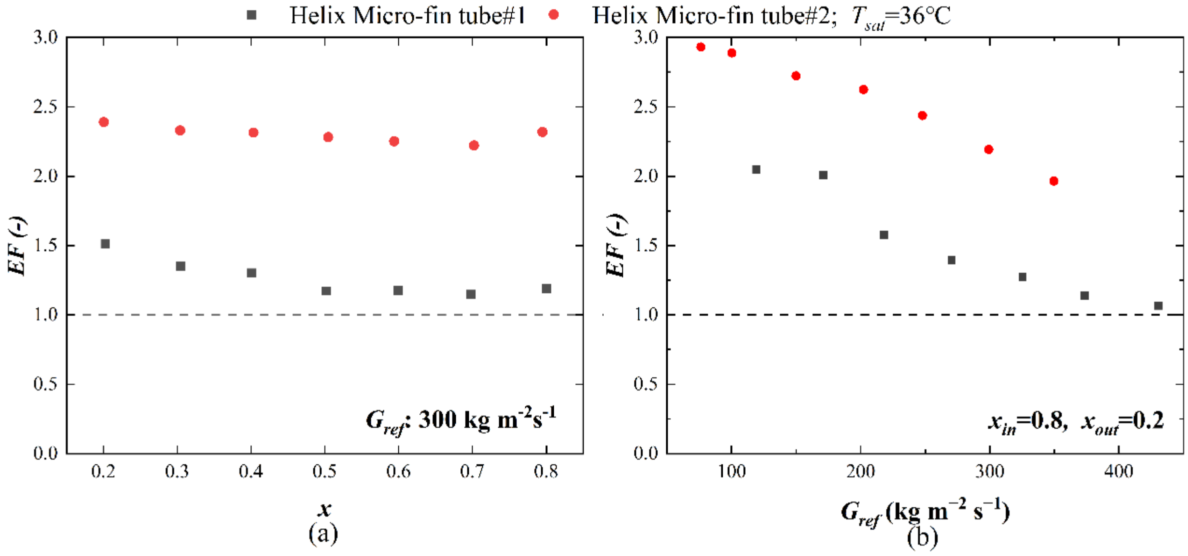

(a)

(b)

Fig. 10. Comparison of enhancement factors (EF) of two enhanced tubes: (a) Average vapor quality as variable, (b) Mass flux as variable.

Fig. 10 illustrates the variations of EF for tubes with the same diameter under the controlled experimental conditions, where the definition of EF is given in Eq. (6a). As shown in Fig. 10(a), EF exhibits little sensitivity to changes in average vapor quality, with the EF values of HX#1 and HX#2 remaining relatively stable in the range of 1.19–1.51 and 2.22–2.39, respectively. In contrast, Fig. 10(b) reveals a significant downward trend in EF with increasing mass flux, where the EF of HX#1 decreases from 2.05 to 1.07, while that of HX#2 decreases from 2.93 to 1.96. This decreasing trend indicates that at medium and high mass fluxes, the enhancement of forced convection leads to a faster growth rate of the heat transfer coefficient for smooth tubes compared to enhanced tubes. More importantly, the increase in heat transfer area alone is insufficient to fully account for the enhancement effect. According to Table 2, the surface area expansion ratios of HX#1 and HX#2 are 1.66 and 1.93, respectively, while their

EF values (particularly at low mass fluxes) are significantly higher than these ratios. This further confirms that, in addition to the increase in surface area, as discussed in Section 4.4, the effective drainage of the liquid-phase refrigerant induced by the specific geometric structure of the spiral micro-fins and the beneficial changes in two-phase flow patterns of refrigerant are the key synergistic mechanisms for achieving high heat transfer efficiency.

4.6. Comprehensive evaluation

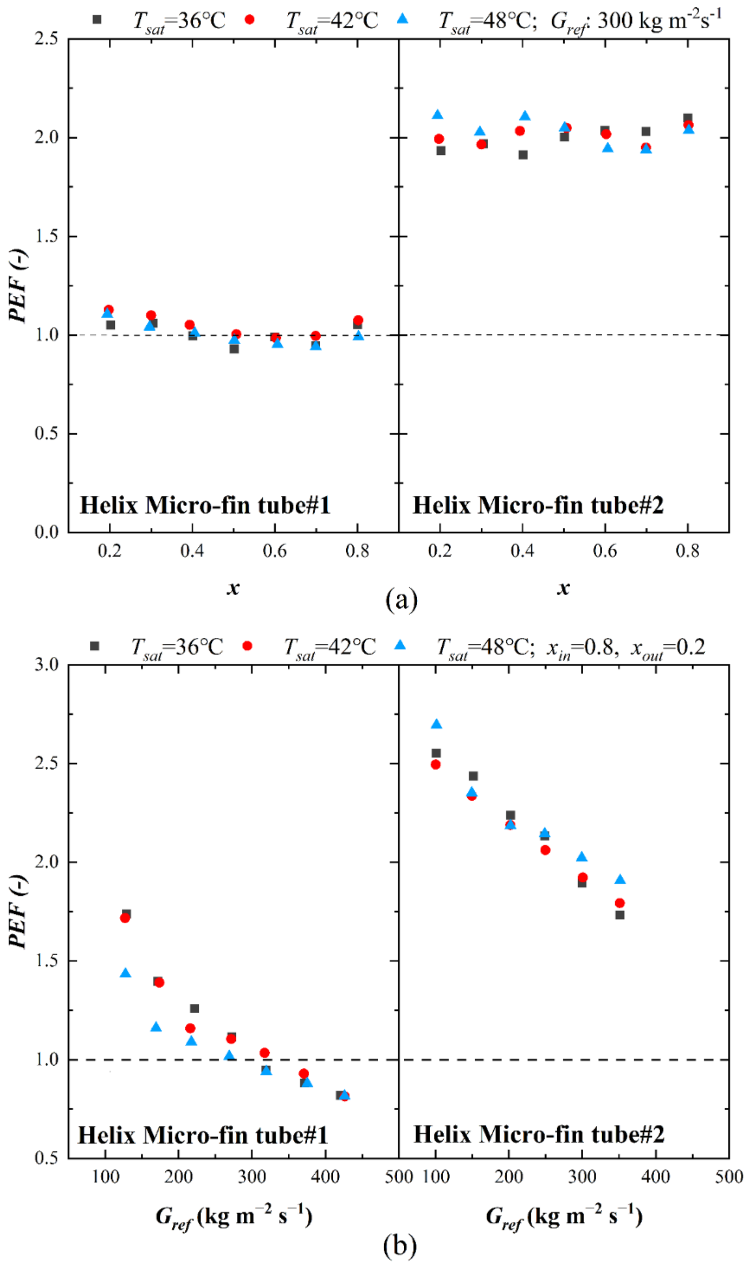

(a)

(b)

Fig. 11. Comparison of performance evaluation factors (PEF) of two enhanced tubes: (a) Average vapor quality as variable, (b) Mass flux as variable.

Fig. 11 illustrates the variations of PEF for tubes with the same diameter under the controlled experimental conditions, where the definition of PEF is given in Eq. (6b). As shown in Fig. 11(a), the PEF value of HX#1 fluctuates around 1.0 (0.93–1.13), while that of HX#2 remains stable at around 2.0 (1.91–2.11). This indicates that heat transfer enhancement and friction dissipation increase synchronously with the average vapor quality. In contrast, as shown in Fig. 11(b), PEF is extremely sensitive to changes in mass flux, exhibiting a negative correlation. As the mass flux increases, the PEF of HX#1 decreases sharply from about 1.7 to 0.8, while that of HX#2 decreases from 2.7 to 1.8. This indicates that at high mass flux, the growth rate of the pressure drop penalty exceeds the gain in heat transfer enhancement. Based on the above analysis, the following conclusions can be drawn: First, in the variable average vapor quality experiment, the comprehensive performance of HX#2 (PEF ≈ 2.0) was consistently superior to that of HX#1 (PEF ≈ 1.0) under the test conditions. In the variable mass flux experiment, the PEF of HX#1 drops below one after the mass flux exceeds approximately 300 kg m^{-2} s^{-1}, indicating that the net performance loss under high mass flux conditions should be considered during application. Second, the insensitivity of PEF to saturation temperature reveals that these two enhanced tubes exhibit a wide range of operational adaptability. Finally, although the geometric structure of HX#1 enhances heat transfer, the excessive pressure drop penalty at high mass flux highlights the need for further optimization of the geometric parameters of small-diameter helix micro-fin tubes to improve their overall performance.

4.7. Predictive Correlation

Table 5

Summary of six current heat transfer coefficient prediction models

Presenter	Content of correlations
Cavallini et al. [32]	$\mathrm{J_G}^{\mathrm{T}} = \left\{\left[\frac{7.5}{4.3X_{tt}^{1.111}+1}\right]^{-3} + C_T^{-3}\right\}^{-\frac{1}{3}}$ $C_T = \begin{cases} 1.6 & Hydrocarbon \\ 2.6 & Other\ refrigerants \end{cases}$ $J_G = \frac{xG}{[gd_h\rho_v(\rho_l-\rho_v)]^{\frac{1}{2}}}$ $J_G > J_G^T$: $h_a = h_{lo}\left[1+1.128x^{0.8170}\left(\frac{\rho_l}{\rho_v}\right)^{0.3685}\left(\frac{\mu_l}{\mu_v}\right)^{0.2363}\left(1-\frac{\mu_l}{\mu_v}\right)^{2.44} Pr_l^{-0.1}\right]$ $J_G \le J_G^T$: $h_d = \left[h_a\left(\frac{J_G^T}{J_G}\right)^{0.8} - h_{start}\right]\left(\frac{J_G}{J_G^T}\right) + h_{start}$, $h_{lo} = \frac{0.023Re_{lo}^{0.8}Pr_l^{0.4}\lambda_l}{D}$

	$h_{start} = 0.725\left[1 + 0.74\left(\frac{1-x}{x}\right)^{0.3321}\right]^{-1}\left[\frac{{\lambda_l}^3\rho_l(\rho_l-\rho_v)gh_{lg}}{\mu_l D\Delta T}\right]^{0.25} + (1 - x^{0.087})h_{lo}$
Moser et al. [33]	$\mathrm{Nu} = \frac{0.0994^{C_1}{Re_l}^{C_2}{Re_{eq}}^{1+0875C_1}{Pr_l}^{0.815}}{\left(1.58\ln Re_{eq} - 3.28\right)\left(2.58\ln Re_{eq} + 13.7{Pr_l}^{2/3} - 19.1\right)}$ $C_1 = 0.126{Pr_l}^{-0.448}, \qquad C_2 = -0.113{Pr_l}^{-0.563}$
Dobson and Chato [34]	$Re_l \leq 1250\text{: } Fr_{so} = 0.025{Re_l}^{1.59}\left(\frac{1+1.09{X_{tt}}^{0.039}}{X_{tt}}\right)\frac{1}{Ga^{0.5}}$ $Re_l > 1250\text{: } Fr_{so} = 1.26{Re_l}^{1.04}\left(\frac{1+1.09{X_{tt}}^{0.039}}{X_{tt}}\right)^{1.5}\frac{1}{Ga^{0.5}}$ $Fr_{so} > 20$: $Nu = 0.023{Re_l}^{0.8}{Pr_l}^{0.4}\left[1 + \frac{2.22}{{X_{tt}}^{0.89}}\right]$ $Fr_{so} < 20$: $Nu = \frac{0.23{Re_{vo}}^{0.12}}{1 + 1.11{X_{tt}}^{0.58}}\left[\frac{GaPr_l}{Ja_l}\right]^{0.25} + \left(1 - \frac{\theta_l}{\pi}\right)0.0195{Re_l}^{0.8}{Pr_l}^{0.4}\sqrt{1.376 + \frac{7.242}{{X_{tt}}^{1.655}}}$ $1 - \frac{\theta_l}{\pi} \cong \frac{arccos(2\alpha - 1)}{\pi}, \qquad \alpha = \left[1 + \frac{1-x}{x}\left(\frac{\rho_v}{\rho_l}\right)^{2/3}\right]^{-1}$
Cavallini and Zecchin [35]	$\mathrm{Nu} = 0.05{Re_{eq}}^{0.8}{Pr_l}^{0.33}$ $\mathrm{Re}_{eq} = Re_v\left(\frac{\mu_v}{\mu_l}\right)\left(\frac{\rho_l}{\rho_v}\right)^{0.5} + Re_l$
Shah et al. [36]	$h_{tp} = 0.023{Re_l}^{0.8}{Pr_l}^{0.4}\frac{k_l}{D_i}\left[(1-x)^{0.8} + \frac{3.8x^{0.76}(1-x)^{0.04}}{{Pr_l}^{0.38}}\right]$
Haraguchi et al. [37]	$\mathrm{Nu} = \left(\mathrm{Nu}_F + \mathrm{Nu}_B\right)^{1/2}$ $Nu_F = 0.0152\left(1 + 0.6{Pr_l}^{0.8}\right)\left(\frac{\Phi_V}{X_{tt}}\right){Re_l}^{0.77}$ $Nu_B = 0.725H(\alpha)\left(\frac{GaPr_L}{H_L}\right)^{1/4}$ $H(\varepsilon) = \varepsilon + \{10[(1-\varepsilon)^{0.1} - 1] + 1.7 \times 10^{-4}Re\}\sqrt{\varepsilon}\left(1 - \sqrt{\varepsilon}\right)$ $\varepsilon = \left[1 + \frac{\rho_v}{\rho_l}\left(\frac{1-x}{x}\right)\left(0.4 + 0.6\sqrt{\frac{\frac{\rho_l}{\rho_v} + 0.4\frac{1-x}{x}}{1 + 0.4\frac{1-x}{x}}}\right)\right]^{-1}$

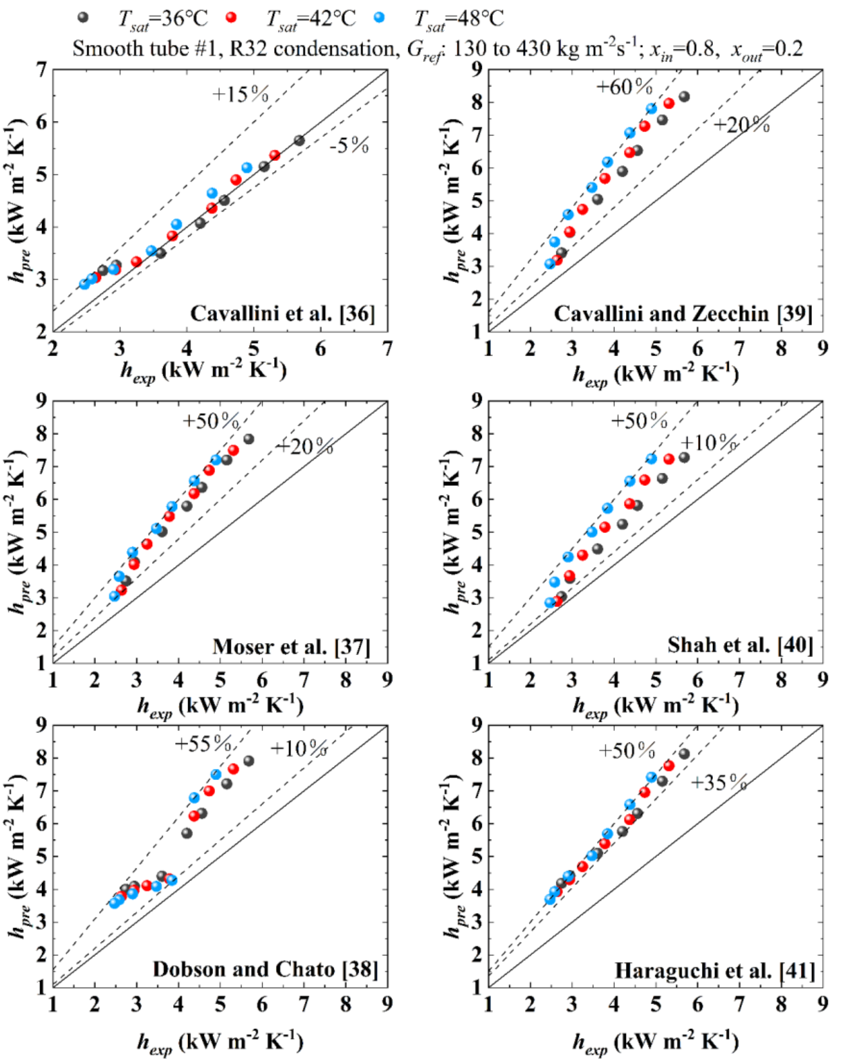

Fig. 12. Comparison of heat transfer coefficients of smooth tube at saturation temperatures of 36 °C, 42 °C, and 48 °C with six predicted models.

Table 6 Deviation between calculated and experimental values of heat transfer coefficients

HTC Correlations	MRE(%)			Average	MAE(%)			Average
	36℃	42℃	48℃	\	36℃	42℃	48℃	\
Cavallini et al. [32]	2.7	4.54	8.95	**5.4**	4.9	4.63	8.95	**6.17**
Shah et al. [36]	23.72	30.36	40.98	**31.69**	23.72	30.36	40.98	**31.69**
Dobson and Chato [34]	37.16	36.26	36.75	**36.72**	37.16	36.26	36.75	**36.72**
Moser et al. [33]	37.34	39.29	44.41	**40.35**	37.34	39.29	44.41	**40.35**
Cavallini and Zecchin [35]	39.07	43.77	52.1	**44.98**	39.07	43.77	52.1	**44.98**
Haraguchi et al. [37]	43.38	45	49.64	**46**	43.38	45	49.64	**46**

As shown in Fig. 12, the predictions of six existing correlations for ST#1 are compared with the corresponding experimental data. Table 5 lists these six correlations, while Table 6 presents their mean relative error (MRE) and mean absolute error (MAE). The deviations between the experimental data and the predictions exhibit distinct trends: although certain datasets show substantial discrepancies, some consistency between predictions and measurements is still observed. Moreover, Table 6 clearly indicates that increasing the saturation temperature leads to larger prediction errors. Considering the flow pattern transition analysis in Section 4.2, we infer that this phenomenon may be attributed to the influence of saturation temperature on the two-phase refrigerant flow field distribution. The correlation developed by Dobson and Chato[34], which is based on the relationship between heat transfer coefficient and two-phase flow regime, shows relatively large overall errors; however, its performance remains nearly insensitive to saturation temperature variation. By contrast, the model proposed by Haraguchi et al. [37] yields the largest discrepancy with the experimental data, with most predictions overestimating the heat transfer coefficient and lying within the +40% error band (MRE = 43.35%, MAE = 43.35%). The best-performing model for smooth tube data in this study is that of Cavallini et al. [32], in which the majority of predicted points fall within the ±20% error band, showing a concentrated distribution and good agreement with the experimental trends (MRE = 2.7%, MAE = 4.9%).

The applicability range of Cavallini et al.'s [32] model covers the refrigerant R32 used in this work and includes a detailed classification of fluid flow patterns, which may account for its high prediction accuracy. When all other conditions are constant, refrigerant type can affect the heat transfer coefficient—for instance, under identical conditions, R32 exhibits slightly higher heat transfer coefficients than R410A[26]. Therefore, model selection must consider the refrigerant applicability. Furthermore, Cavallini et al. [32] established a criterion to classify the flow patterns in the prediction process; its accuracy has also been confirmed in previous work by Mattiuzzo et al. [29].

Accordingly, in the subsequent part of this section, a modified prediction model tailored to the enhanced tubes in this experiment will be developed based on the Cavallini et al. [32] framework.

4.7.2. Modification of the correlation

This study first validated the classical Cavallini model [32]. As shown in Fig. 13(a), the predictions of this model deviate significantly from the experimental data, with all data points falling within the range of –67% to –5%, indicating a severe underestimation of the condensation heat transfer performance in the helix micro-fin tubes employed in this study. In light of this, the corrected model subsequently proposed by Cavallini et al. [38] was further examined. As illustrated in Fig. 13(b), the modified model markedly improves the prediction accuracy for the large-diameter tube (HX#2), with the deviation range narrowed to –25% to +10%. However, its applicability to the small-diameter tube (HX#1) remains limited, as the model substantially overestimates the heat transfer coefficient, yielding prediction errors in the range of +30% to +60%. Since none of the existing models can simultaneously and accurately predict the heat transfer coefficients for both tube diameters, the subsequent part of this section develops a modified correlation based on the experimental data to address this limitation.

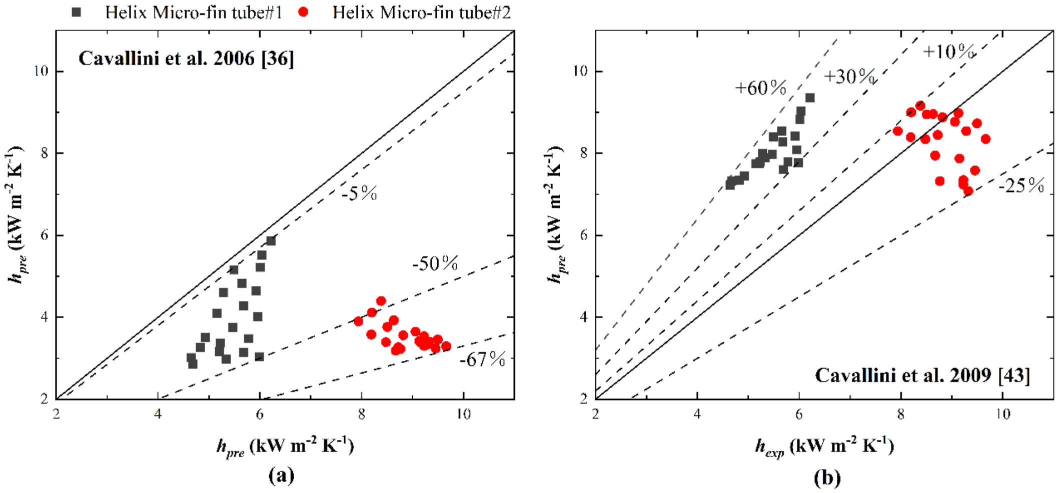

Fig. 13. Predictions of condensation data in enhanced tubes using existing correlations: (a) proposed by Cavallini et al. (2006) [32], (b) proposed by Cavallini et al. (2009) [38].

Based on the flow pattern analysis presented in Section 4.1, the transition dimensionless gas velocity ($J_G{}^T$) used by Cavallini et al. [32] was modified, as illustrated in Fig. 14, to improve the accuracy in the determination of flow patterns inside HX tubes with different geometries. The modified expression is given in Eq. (8).

$$J_{v,e}^{T} = 0.9\left\{\left[\frac{7.1}{5.1X_{tt}^{1.111}+1}\right]^{-3} + 2.5^{-3}\right\}^{-1/3} \quad if\ D_i < 0.006 \tag{8a}$$

$$J_{v,e}^{T} = 0.8\left\{\left[\frac{3.06}{1.34X_{tt}^{1.111}+1}\right]^{-3} + 2.5^{-3}\right\}^{-1/3} \quad if\ D_i \geq 0.006 \tag{8b}$$

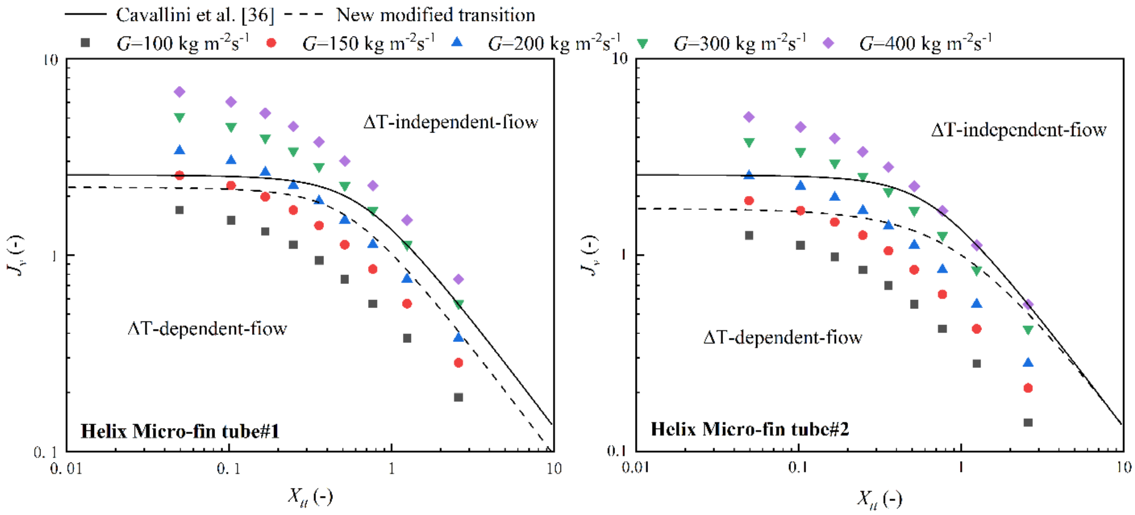

Fig. 14. Modification of the JGT used in Cavallini et al. [32].

The effective heat transfer performance of helix micro-fin tubes depends on fluid characteristics, flow pattern distribution, heat flow direction (evaporation or condensation), and tube geometry. In this study, the existing model was modified according to the phenomena observed in the experiments. The modification focuses on two core factors: i) Flow pattern distribution — Based on the analysis of flow field variations in Section 4.1, the Froude rate (*Ft*) was introduced. ii) Tube geometry — Based on the analysis in Section 4.3.1 of the heat transfer performance of the helical micro-fin tubes across different mass flux ranges, and with reference to the work of Marto et al. [39] on the influence of micro-fin tube geometry on the heat transfer coefficient, the area enhancement ratio (*Ar*) and the fin pitch-to-height ratio (p_t/e) were introduced. On this basis, a new semi-empirical model is proposed. This model adopts the modified correlation of Cavallini et al. [38] as its framework, retaining its description of the effect of fin number (expressed via factor *C*) on heat transfer. Meanwhile, to more accurately capture the changes in flow patterns and the specific effects induced by micro-geometric structures, the above three dimensionless parameters — *Ft*, *Ar*, and p_t/e— were incorporated to replace certain empirical terms in the original model. The undetermined empirical coefficients were obtained using an interior-point algorithm by solving a composite objective function subject to multiple physical constraints. The final modified correlation is presented in Table 7.

Table 7 Final modified correlation for predicting the heat transfer coefficient.

	Content of correlation
New modified correlation	$h = [h_A^{1.367} + h_D^{1.367}]^{1/1.367}$ $h_A = h_{AS} A \cdot C$ $h_{AS} = h_{LO}\left[1 + 1.128x^{0.817}\left(\frac{\rho_l}{\rho_v}\right)^{0.3685}\left(\frac{\mu_l}{\mu_v}\right)^{0.2363}\left(1-\frac{\mu_v}{\mu_l}\right)^{2.144}\mathrm{Pr}_l^{-0.1}\right]$ $h_{LO} = 0.023\frac{\lambda_L}{D_i}\left(\frac{GD_i}{\mu_L}\right)^{0.8} Pr_l^{0.4}$ $A = 0.4251 + 2.35Ft^{-0.7643}Ar^{3.98}\left(\frac{p_t}{e}\right)^{-2.72}$ $Ft = \{(G^2x^3)/[(1-x)\rho_v^2 gD_i]\}^{1/2}$ $C = 1 \text{ if } (e_{\mathrm{opt}}/e_{\mathrm{g}}) \geq 0.8\ ; C = (e_{\mathrm{opt}}/e_{\mathrm{g}})^{1.904} \text{ if } (e_{\mathrm{opt}}/e_{\mathrm{g}}) < 0.8\ ;$ $n_{\mathrm{opt}} = 4064.4D_i + 23.257$ $h_D = C\left[1 + 0.02123x^{1.017}Ar^{3.185}\left(\frac{p_t}{e}\right)^{-1.393}C_1^{-2.186}\right]h_{D,S} + C\left[Ar^{-2.158}\left(\frac{p_t}{e}\right)^{0.7767}\right](1-x^{0.087})h_{LO}$ $h_{D,S} = \frac{0.725}{1+0.741\left[\frac{1-x}{x}\right]^{0.3321}}\left[\frac{\lambda_l^3 \cdot \rho_l(\rho_l-\rho_v)g \cdot h_{lv}}{\mu_l \cdot D_i \cdot \Delta T}\right]^{0.25}$ $C_1 = 1\ if\ J_v \geq J_{v,e}^T\ ;\ \ C_1 = (J_v/J_{v,e}^T)\ if\ J_v < J_{v,e}^T$ $J_{v,e}^T = 0.9\left\{\left[\frac{7.1}{5.1X_{tt}^{1.111}+1}\right]^{-3} + 2.5^{-3}\right\}^{-1/3} \quad if\ D_i < 0.006$

$$J_{v,e}^{T}=0.8\left\{\left[\frac{3.06}{1.34X_{tt}^{1.111}+1}\right]^{-3}+2.5^{-3}\right\}^{-1/3}\quad if\ D_i\geq 0.006$$

Fig. 15 presents the prediction performance of the new correlation proposed in this study. The model exhibits excellent predictive capability for both tube diameters. For the small tube diameter (HX#1), all data points converge precisely within an error band of ±15%, with an MRE of only +0.7% and an MAE of +7.1%. For the large tube diameter (HX#2), the predictions are likewise in close agreement with the experimental data, with deviations maintained within the range of −20% to +15%, and corresponding MRE and MAE values of −3.2% and +7.2%, respectively. These results demonstrate that the new correlation not only preserves the high-accuracy prediction of the heat transfer coefficient for large tube diameters but, more importantly, also successfully eliminates the substantial overprediction of the heat transfer coefficient for small tube diameters present in the previous model. This provides strong validation of the effectiveness of our proposed modification strategy.

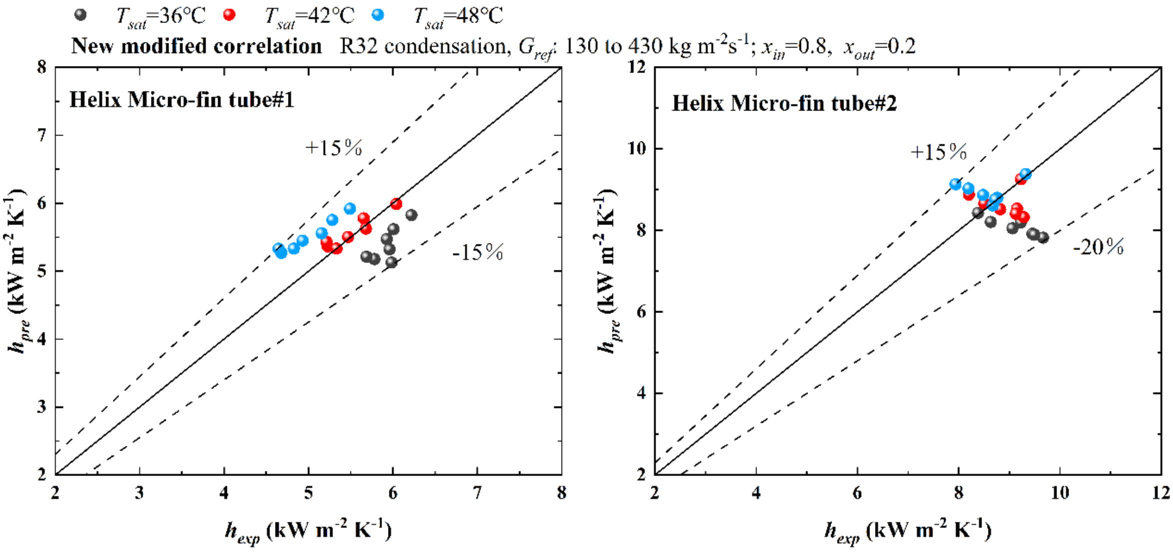

Fig. 15. Prediction performance of the new correlation for condensation heat transfer coefficients in helix micro-fin tubes.

5. Conclusions

The flow condensation characteristics of R32 in smooth tubes with outer diameters of 5 mm and 9.52 mm, as well as in helix micro-fin tubes, were experimentally investigated. The results include condensation heat transfer coefficients, pressure drops, and their correlations. The main conclusions are as follows:

1. During flow condensation, both the in-tube heat transfer coefficient and the frictional pressure drop generally increase with increasing mass flux. Notably, however, the heat transfer coefficient of HX#2 exhibits an opposite trend. This can be

attributed to the progressive submergence of the fins by the liquid film as mass flux increases, which weakens their disturbance effect on the fluid. The influence of saturation temperature on heat transfer and pressure drop is primarily due to changes in the thermophysical properties of the refrigerant, leading to a consistent trend among the four tested tubes—both parameters decrease with increasing saturation temperature.

2. Regarding the effect of tube diameter in different tube structures, with the increase in mass flux, the heat transfer performance of ST#2 and ST#1 alternately leads. However, for the helical micro-fin tubes employed in this study, HX#2 (EF ranging from 1.96 to 2.93) demonstrates consistently superior performance compared with HX#1 (EF ranging from 1.07 to 2.05). In both cases, EF decreases with increasing mass flux, indicating that the rate of increase in the heat transfer coefficient for smooth tubes is greater than that for helix micro-fin tubes. Regarding variations in average vapor quality, smooth tubes and helix micro-fin tubes exhibit consistent trends.
3. The present study evaluates the enhanced tubes using PEF. Experimental results show that with increasing mass flux, the PEF of HX#1 decreases from 1.7 to 0.8, whereas the PEF of HX#2 decreases uniformly from 2.7 to 1.8. This indicates that although the helix micro-fin structure improves heat transfer performance, it also induces greater frictional dissipation. Both tubes show favorable overall performance in the low mass flux range, leading to the conclusion that the helix micro-fin structure used in this study is more suitable for larger tube diameters (9.52 mm).
4. Six existing correlations were used to evaluate the heat transfer performance of the smooth tube, among which the correlation of Cavallini et al. (2006) provided the highest accuracy, with an MAE of 3.97%. However, for helix micro-fin tubes, existing modified correlations exhibited substantial deviations. To address this, a new predictive model was established, within the framework of the Cavallini et al. modified model by incorporating dimensionless parameters related to flow pattern distribution and geometric configuration. This correlation achieved high-accuracy, unified prediction of heat transfer coefficients for different tube diameters, with MRE values of +0.7% and −3.2% and MAE values of +7.1% and +7.2% for the small- and large-diameter tubes, respectively.

Nomenclature

A	area, m^2
Ar	area expansion ratio
c_p	specific heat, J kg^{-1} K^{-1}
D	diameter, m

Greek letters

β	helix angle, ◦
γ	apex angle, ◦
ε	void fraction
λ	thermal conductivity, W m^{-1} K^{-1}

e	fin height, m
f	Fanning friction factor
Ft	Froude rate, dimensionless
g	Standard gravitational acceleration, m s^{-2}
G	mass flux, kg m^{-2} s^{-1}
Ga	Galileo number
h	heat transfer coefficient, W m^{-2} K^{-1}
h_{lv}	latent heat of vaporization, J kg^{-1}
J_G	dimensionless gas velocity
L	tube length, m
LMTD	logarithmic mean temperature, K
m	mass flow rate, kg s^{-1}
n_f	number of fins
Nu	Nusselt number
p_t	fin pitch
P	pressure, kpa
Pr	Prandtl number
q	heat flux, W m^{-2}
Q	heat flow, W
Re	Reynolds number
T	temperature, K
We	Weber number
x	vapor quality
Xtt	Lockhart-Martinelli parameter

μ	dynamic viscosity, Pa s
ρ	density, kg m^{-3}
σ	surface tension, N m^{-1}

Subscripts

bulk	bulk temperature
e	enhanced tubes
exp	experimental
i	inner
in	inlet
l	liquid phase
lo	liquid phase with total flow
o	outer
out	outlet
ph	preheating section
ref	refrigerant
s/st	smooth tube
sat	saturation condition
to	total
tp	two-phase
v	vapor phase
w	water

References

[1] F. Yang, X. Yang, X. Li, China's diverse energy transition pathways toward carbon neutrality by 2060, Sustain. Prod. Consum. 47 (2024) 236–250, https://doi.org/10.1016/j.spc.2024.04.007.

[2] A. Kumar, R. Kumar, A.K. Das, Two-phase flow condensation heat transfer characteristics of R-134a inside three-dimensional cylindrical micropillar enhanced tube, Int. J. Refrig. 159 (2024) 88–98, https://doi.org/10.1016/j.ijrefrig.2023.12.029.

[3] W. Li, W. Feng, X. Liu, J. Li, B. Cao, B. Dou, et al., Condensation heat transfer and pressure drop characteristics inside smooth and enhanced tubes with R410A and R32, Int. J. Heat Mass Transf. 214 (2023) 124419, https://doi.org/10.1016/j.ijheatmasstransfer.2023.124419.

[4] W. Li, J. Wang, Y. Guo, Q. Shi, Y. He, D.J. Kukulka, et al., R410A flow condensation inside two dimensional micro-fin tubes and three dimensional dimple tubes, Int. J. Heat Mass Transf. 182 (2022) 121910, https://doi.org/10.1016/j.ijheatmasstransfer.2021.121910.

[5] X. Wang, W. Li, L. Zhang, J. Wu, J. Zhang, D.J. Kukulka, et al., Condensation characteristics of flows in newly developed three-dimensional enhanced heat transfer tubes, Energy 305 (2024) 132114, https://doi.org/10.1016/j.energy.2024.132114.

[6] J. Choi, S. Kwon, M. Lee, C. Han, J. Kim, D. Lee, et al., Comparative experimental evaluation on condensation heat transfer characteristics of R466A and R410A in smooth and micro-fin tubes, Int. Commun. Heat Mass Transf. 159 (2024) 108247, https://doi.org/10.1016/j.icheatmasstransfer.2024.108247.

[7] Z. Lu, J. Jiang, C. Tang, L. Tao, J. Chen, Z. Zheng, et al., Research on the R513A condensation heat transfer characteristics in horizontal microfin tubes, Int. Commun. Heat Mass Transf. 154 (2024) 107462, https://doi.org/10.1016/j.icheatmasstransfer.2024.107462.

[8] J.V.W. Kühl, F.G. Palm, J. Dietl, J. El-Hajal, A. Gotterbarm, M.H. Rausch, et al., Influence of surface structure and tube material on the condensation heat transfer coefficient of n-butane on horizontal single tubes and in tube bundles, Int. J. Heat Mass Transf. 233 (2024) 125973, https://doi.org/10.1016/j.ijheatmasstransfer.2024.125973.

[9] A. Diani, Y. Liu, J. Wen, L. Rossetto, Experimental investigation on the flow condensation of R450A, R515B, and R1234ze(E) in a 7.0 mm OD micro-fin tube, Int. J. Heat Mass Transf. 196 (2022) 123260, https://doi.org/10.1016/j.ijheatmasstransfer.2022.123260.

[10] M. Hirose, J. Ichinose, N. Inoue, Development of the general correlation for condensation heat transfer and pressure drop inside horizontal 4 mm small-diameter smooth and microfin tubes, Int. J. Refrig. 90 (2018) 238–248, https://doi.org/10.1016/j.ijrefrig.2018.04.014.

[11] Y. Hu, S.A. Jajja, C.-M. Yang, S.F. Yana Motta, B.A. Fricke, K. Nawaz, In tube condensation of low global warming potential refrigerants in an axial micro-fin aluminum tube, Int. J. Refrig. 161 (2024) 221–241, https://doi.org/10.1016/j.ijrefrig.2024.03.001.

[12] T. Arkadumnuay, S. Manova, W. Leunanonchai, L.G. Asirvatham, S. Wongwises, Experimental investigation on the condensation heat transfer coefficient and frictional pressure drop of R-513A and R-134a in commercial refrigeration tubes, Int. J. Heat Mass Transf. 229 (2024) 125735, https://doi.org/10.1016/j.ijheatmasstransfer.2024.125735.

[13] Q. Li, G. Chen, Q. Wang, L. Tao, Y. Xuan, Theoretical and experimental analyses of two-phase flow condensation heat transfer inside the horizontal micro-fin tube, Appl. Therm. Eng. 216 (2022) 119066, https://doi.org/10.1016/j.applthermaleng.2022.119066.

[14] L. Qingpu, C. Guangming, W. Qin, T. Leren, X. Yongmei, Experimental study of condensation heat transfer of R134a inside the micro-fin tubes at high mass flux, Int. J. Heat Mass Transf. 187 (2022) 122524, https://doi.org/10.1016/j.ijheatmasstransfer.2022.122524.

[15] S.G. Holagh, M.A. Abdous, H. Rastan, M. Shafiee, M. Hashemian, Performance analysis of micro-fin tubes compared to smooth tubes as a heat transfer enhancement technique for flow condensation, Energy Nexus 8 (2022) 100154, https://doi.org/10.1016/j.nexus.2022.100154.

[16] Q. Li, X. Meng, L. Li, N. Gao, N. Li, R. Qiu, An experimental study of annular film flow condensation in a micro-fin tube with high mass flux, Int. J. Refrig. 160 (2024) 106–118, https://doi.org/10.1016/j.ijrefrig.2024.01.024.

[17] A. Diani, A. Cavallini, L. Rossetto, R1234yf condensation inside a 3.4 mm ID horizontal microfin tube, Int. J. Refrig. 75 (2017) 178–189, https://doi.org/10.1016/j.ijrefrig.2016.12.014.

[18] A. Diani, M. Campanale, L. Rossetto, Experimental study on heat transfer condensation

of R1234ze(E) and R134a inside a 4.0 mm OD horizontal microfin tube, Int. J. Heat Mass Transf. 126 (2018) 1316–1325, https://doi.org/10.1016/j.ijheatmasstransfer.2018.06.047.

[19] J. Zhang, N. Zhou, W. Li, Y. Luo, S. Li, An experimental study of R410A condensation heat transfer and pressure drops characteristics in microfin and smooth tubes with 5 mm OD, Int. J. Heat Mass Transf. 125 (2018) 1284–1295, https://doi.org/10.1016/j.ijheatmasstransfer.2018.04.128.

[20] M. Khairul Bashar, K. Nakamura, K. Kariya, A. Miyara, Development of a correlation for pressure drop of two-phase flow inside horizontal small diameter smooth and microfin tubes, Int. J. Refrig. 119 (2020) 80–91, https://doi.org/10.1016/j.ijrefrig.2020.08.013.

[21] G.A. Longo, S. Mancin, G. Righetti, C. Zilio, Comparative analysis of microfin vs smooth tubes in R32 and R410A condensation, Int. J. Refrig. 128 (2021) 218–231, https://doi.org/10.1016/j.ijrefrig.2021.04.011.

[22] N. Irannezhad, L. Rossetto, A. Diani, A comprehensive study with high-speed camera assisted visualizations of HFO-1234ze(E) condensation inside an enhanced tube, Int. Commun. Heat Mass Transf. 150 (2024) 107203, https://doi.org/10.1016/j.icheatmasstransfer.2023.107203.

[23] H. Ubudiyah, A.K. Mainil, K. Kariya, A. Miyara, Experimental study and general correlation for condensation heat transfer coefficient inside microfin tubes, Int. J. Refrig. 158 (2024) 422–430, https://doi.org/10.1016/j.ijrefrig.2023.11.017.

[24] S.Z. Rouhani, E. Axelsson, Calculation of void volume fraction in the subcooled and quality boiling regions, Int. J. Heat Mass Transf. 13 (1970) 383 – 393, https://doi.org/10.1016/0017-9310(70)90114-6.

[25] R.J. Moffat, Describing the uncertainties in experimental results, Exp. Therm. Fluid Sci. 1 (1) (1988) 3–17, https://doi.org/10.1016/0894-1777(88)90043-X.

[26] L. Ma, X. Liu, Y. Gao, W. Li, Z. Wu, X. Luo, et al., R410A and R32 condensation heat transfer and flow patterns inside horizontal micro-fin and 3-D enhanced tubes, Int. Commun. Heat Mass Transf. 142 (2023) 106638, https://doi.org/10.1016/j.icheatmasstransfer.2023.106638.

[27] J. El Hajal, J.R. Thome, A. Cavallini, Condensation in horizontal tubes, part 1: two-phase flow pattern map, Int. J. Heat Mass Transf. 46 (2003) 3349–3363, https://doi.org/10.1016/S0017-9310(03)00139-X.

[28] C. Liu, F. Wang, Y. Gao, Y. Zheng, R. Li, Numerical analysis and correlation comparison of void fraction in refrigerant two-phase flow in horizontal tube, Appl. Therm. Eng. 270 (2025) 126276, https://doi.org/10.1016/j.applthermaleng.2025.126276.

[29] N. Mattiuzzo, M. Azzolin, A. Berto, S. Bortolin, D. Del Col, Condensation heat transfer and pressure drop of R1234yf/HFC mixtures inside small diameter channels, Int. J. Therm. Sci. 189 (2023) 108258, https://doi.org/10.1016/j.ijthermalsci.2023.108258.

[30] E.T. Hurlburt, T.A. Newell, Modeling of the Evaporation and Condensation of Zeotropic Refrigerant Mixtures in Horizontal Annular Flow, ACRC TR-129, Air Conditioning and Refrigeration Center, University of Illinois, Urbana, 1997, http://hdl.handle.net/2142/11632.

[31] L. Liebenberg, J.R. Thome, J.P. Meyer, Flow Visualization and Flow Pattern Identification With Power Spectral Density Distributions of Pressure Traces During Refrigerant Condensation in Smooth and Microfin Tubes, J. Heat Transf. 127 (2005) 209–220,

https://doi.org/10.1115/1.1857942.

[32] A. Cavallini, D.D. Col, L. Doretti, M. Matkovic, L. Rossetto, C. Zilio, et al., Condensation in Horizontal Smooth Tubes: A New Heat Transfer Model for Heat Exchanger Design, Heat Transf. Eng. 27 (2006) 31–38, https://doi.org/10.1080/01457630600793970.

[33] K.W. Moser, R.L. Webb, B. Na, A New Equivalent Reynolds Number Model for Condensation in Smooth Tubes, J. Heat Transf. 120 (1998) 410–417, https://doi.org/10.1115/1.2824265.

[34] M.K. Dobson, J.C. Chato, Condensation in Smooth Horizontal Tubes, J. Heat Transf. 120 (1998) 193–213, https://doi.org/10.1115/1.2830043.

[35] A. Cavallini, R. Zecchin, A dimensionless correlation for heat transfer in forced convection condensation. In: Fith Int. Heat Transf. Conf. , Tokyo, 3, 1974, pp. 309–313.

[36] M.M. Shah, A general correlation for heat transfer during film condensation inside pipes, Int. J. Heat Mass Transf. 22 (1979) 547–556, https://doi.org/10.1016/0017-9310(79)90058-9.

[37] H. Haraguchi, S. Koyama, T. Fujji, Condensation of refrigerants HCFC22, HFC134a and HCFC123 in a horizontal smooth tube: 2nd report, proposals of empirical expressions for local heat transfer coefficient, Trans. Jpn. Soc Mech. Eng. 60 (1994) 245 – 252, https://www.osti.gov/etdeweb/biblio/6727038.

[38] A. Cavallini, D. Del Col, S. Mancin, L. Rossetto, Condensation of pure and near-azeotropic refrigerants in microfin tubes: A new computational procedure, Int. J. Refrig. 32 (2009) 162–174, https://doi.org/10.1016/j.ijrefrig.2008.08.004.

[39] P.J. Marto, D. Zebrowski, A.S. Wanniarachchi, J.W. Rose, An Experimental Study of R-113 Film Condensation on Horizontal Integral-Fin Tubes, J. Heat Transf. 112 (1990) 758–767, https://doi.org/10.1115/1.2910451.